

Exterior complex scaling enables physics-informed neural networks for quantum scattering

Jin Lei^{1,*}

¹*School of Physics Science and Engineering, Tongji University, Shanghai 200092, China.*

(Dated: February 5, 2026)

Physics-informed neural networks (PINNs) have emerged as a powerful tool for solving differential equations, yet their application to quantum scattering problems has been hindered by the oscillatory, non-decaying nature of scattering wave functions. In this work, I demonstrate that exterior complex scaling (ECS) transforms scattering boundary conditions into exponentially decaying waves suitable for neural network solutions, enabling PINNs to solve nuclear scattering problems for the first time. I develop a driven-equation formulation where the source term is confined to the real axis, avoiding the need to analytically continue nuclear potentials into the complex plane. The method is validated on nucleon-nucleus scattering ($n+^{40}\text{Ca}$ at $E_{\text{lab}} = 20$ MeV) with 21 partial waves, achieving phase shift accuracy of $\Delta\delta < 0.1^\circ$ for most channels when compared to conventional solvers. I further demonstrate the approach on heavy-ion scattering ($^6\text{Li}+^{208}\text{Pb}$ at 40 MeV) with 41 partial waves and strong Coulomb effects. This work establishes the foundation for extending PINNs to inverse problems where end-to-end differentiability enables direct fitting of optical potential parameters, coupled-channel reactions, and few-body scattering where traditional grid methods face exponential scaling.

I. INTRODUCTION

Nuclear scattering experiments provide fundamental information about nuclear structure and reaction mechanisms that underpin our understanding of atomic nuclei. When a beam of particles strikes a target nucleus, the angular distribution of scattered particles encodes information about the nuclear potential through which the projectile propagates. This potential, known as the optical model potential, contains both real components describing elastic scattering and imaginary components accounting for absorption into non-elastic channels such as compound nucleus formation, direct reactions, and particle emission. Extracting nuclear structure information from scattering data requires solving the quantum mechanical scattering problem, typically formulated as a partial-wave decomposition of the Schrödinger equation with appropriate boundary conditions at infinity [1, 2].

The computational challenge of nuclear scattering lies not in the differential equation itself, which is a straightforward second-order ordinary differential equation, but rather in the boundary conditions. Unlike bound-state problems where the wave function decays exponentially at large distances, scattering wave functions remain oscillatory at all radii, behaving asymptotically as linear combinations of incoming and outgoing spherical waves. Traditional numerical methods must propagate solutions to sufficiently large radii where the nuclear potential vanishes, then match to known asymptotic forms to extract phase shifts and S-matrix elements. For systems with long-range Coulomb interactions, this matching becomes particularly delicate because the Coulomb potential extends to infinity and modifies the asymptotic behavior in

nontrivial ways involving logarithmic phase corrections.

Physics-informed neural networks have recently emerged as a powerful paradigm for solving differential equations by training neural networks to minimize residuals of the governing equations at collocation points [3–5]. Unlike traditional numerical methods that discretize the computational domain, PINNs represent solutions as continuous, differentiable functions parameterized by network weights. This approach has proven successful for a wide range of problems in fluid mechanics, heat transfer, and solid mechanics, particularly for stationary problems. More broadly, neural networks have demonstrated remarkable capability in solving quantum mechanical problems, including variational solutions of the many-body Schrödinger equation [6–8]. The key advantage of PINNs is their mesh-free nature and ability to incorporate physics constraints directly into the loss function, making them attractive for problems with complex geometries or those where generating high-quality meshes is challenging. Libraries such as DeepXDE [9] have made these methods increasingly accessible.

Despite their success in many domains, PINNs face a fundamental obstacle when applied to scattering problems. Scattering wave functions satisfy radiation boundary conditions (Sommerfeld conditions) at infinity, requiring the solution to be a specific superposition of incoming and outgoing waves. These conditions cannot be reduced to simple Dirichlet or Neumann conditions at any finite boundary because the wave function oscillates indefinitely and the correct asymptotic form involves the unknown phase shift that one is trying to compute. Truncating the computational domain at any finite radius introduces spurious reflections that contaminate the solution. This fundamental incompatibility between oscillatory radiation conditions and finite-domain computation has prevented the application of PINNs to scattering problems in nuclear and atomic physics.

* jinl@tongji.edu.cn

Exterior complex scaling provides an elegant solution to this boundary condition problem by analytically continuing spatial coordinates into the complex plane beyond a certain radius [10–13]. When the radial coordinate r is rotated into the complex plane by an angle θ , outgoing waves that behave as e^{ikr} become exponentially damped as $e^{ikr \cos \theta} e^{-kr \sin \theta}$. This transformation converts the scattering problem into one with square-integrable (L^2) boundary conditions: the wave function now decays exponentially at large distances and can be set to zero at a finite outer boundary, serving a similar purpose to perfectly matched layer absorbing boundaries [14] that have also been adapted for quantum wave equations [15]. The physics of the scattering process is preserved because the complex scaling only affects the asymptotic region where the potential vanishes, leaving the nuclear interaction region on the real axis where wave functions and observables are physically meaningful.

The application of complex scaling to scattering calculations was pioneered in atomic and molecular physics for studying resonances and electron-atom collisions [16]. In nuclear physics, complex scaling has been applied to study resonances in light nuclei [17]. In nuclear physics, Liu, Lei, and Ren recently developed the COLOSS code implementing complex scaling for optical model calculations [18]. These conventional discretization methods (finite differences, R-matrix [19–21], Numerov [22]) are highly efficient for single-channel scattering, and the present work does not aim to replace them for such applications. Rather, the motivation for combining ECS with PINNs lies in the unique advantages that neural network approaches offer for more challenging problems.

The key advantages of a PINN-based scattering solver are threefold. First, the entire computational pipeline is end-to-end differentiable, enabling gradient-based optimization of potential parameters to fit experimental data, i.e., inverse problems that would otherwise require expensive outer-loop optimization over repeated forward solves. Second, PINNs naturally extend to multi-output representations, making coupled-channel calculations conceptually straightforward without explicitly constructing coupled matrix equations. Third, mesh-free neural network methods scale more favorably with dimensionality than grid-based approaches, offering a potential pathway to few-body scattering problems (e.g., Faddeev equations [23–25]) where traditional methods face exponential computational cost. The present work establishes the foundation by validating PINN-ECS against established solvers on well-understood single-channel benchmarks.

I develop a driven-equation formulation for scattering that decomposes the total wave function into an incident wave (a known Coulomb function for charged-particle scattering) and a scattered wave that satisfies an inhomogeneous equation. The source term driving the scattered wave is proportional to the short-range potential (nuclear plus charged-sphere Coulomb correction) times the incident wave, and thus vanishes identically for $r > R_0$ where

both contributions are zero. This means the right-hand side of the driven equation is confined to the real axis, and the scattered wave in the complex-scaled region satisfies a homogeneous equation with decaying boundary conditions, which is precisely the type of problem that PINNs can solve naturally.

Several technical innovations are required to make this approach work reliably. The boundary condition factor that enforces $u(0) = 0$ and $u(R_{\max}) = 0$ must be carefully engineered to avoid numerical pathologies at high angular momentum, where the factor $r^{\ell+1}$ grows rapidly and can suppress the wave function in the nuclear interior. I introduce a sigmoid-capped boundary condition factor that saturates the angular momentum dependence beyond the nuclear radius, preventing this amplification while maintaining the correct behavior near the origin. The extraction of phase shifts from the neural network solution requires computing wave function derivatives accurately. For the scattered wave, I use automatic differentiation provided by the neural network framework, while for the Coulomb functions, I use their known analytic derivative formulas. To improve robustness, the S-matrix is averaged over multiple matching radii.

In this paper, I validate the PINN-ECS method on two benchmark systems. The first is neutron scattering on ^{40}Ca at $E_{\text{lab}} = 20$ MeV using the Koning-Delaroche global optical potential, which includes volume, surface, and spin-orbit terms [26]. I compute 21 partial waves up to $\ell = 10$ and compare phase shifts and S-matrix elements to those obtained from the established COLOSS code. The second benchmark is $^6\text{Li} + ^{208}\text{Pb}$ elastic scattering at 40 MeV, a heavy-ion system with strong Coulomb effects (Sommerfeld parameter $\eta \approx 15$) requiring 41 partial waves. I compute the Rutherford ratio $(d\sigma/d\Omega)/(d\sigma/d\Omega)_{\text{Ruth}}$ and demonstrate the characteristic Coulomb-nuclear interference pattern.

The paper is organized as follows. Section II presents the theoretical framework, including the radial Schrödinger equation, the exterior complex scaling transformation, and the driven-equation formulation for scattering. Section III describes the neural network architecture, loss functions, and training procedure. Section IV presents benchmark results for $n + ^{40}\text{Ca}$ and $^6\text{Li} + ^{208}\text{Pb}$ scattering. Section V discusses the capabilities and limitations of the approach. Section VI summarizes my findings and outlines future directions.

II. THEORETICAL FRAMEWORK

The quantum mechanical description of nuclear scattering begins with the time-independent Schrödinger equation for the relative motion of two colliding nuclei. In the center-of-mass frame, the three-dimensional wave function can be expanded in partial waves, each characterized by orbital angular momentum quantum number ℓ . For each partial wave, the radial wave function $u_\ell(r) = rR_\ell(r)$, where $R_\ell(r)$ is the radial part of the full

wave function, satisfies a one-dimensional Schrödinger equation that forms the starting point of my analysis.

The radial Schrödinger equation in the variable x (the physical radial coordinate) takes the form

$$\left[-\frac{\hbar^2}{2\mu} \frac{d^2}{dx^2} + \frac{\hbar^2 \ell(\ell+1)}{2\mu x^2} + V_N(x) + V_C(x) \right] u(x) = E u(x), \quad (1)$$

where μ is the reduced mass of the projectile-target system, E is the center-of-mass kinetic energy, $V_N(x)$ is the short-range nuclear potential, and $V_C(x)$ is the Coulomb potential arising from the electrostatic repulsion between nuclei with charges Z_1 and Z_2 , modeled as a uniformly charged sphere with radius $R_C = r_C A^{1/3}$ (using $r_C = 1.3$ fm) to avoid the point-charge singularity at the origin. The centrifugal term $\hbar^2 \ell(\ell+1)/(2\mu x^2)$ arises from the angular part of the kinetic energy operator and creates an effective barrier that prevents low-energy particles from penetrating to small radii for high angular momenta. The wave function must satisfy the boundary condition $u(0) = 0$ to remain finite at the origin, and for scattering states at positive energy $E > 0$, it must match the appropriate asymptotic form at large distances.

The nuclear potential $V_N(x)$ in optical model calculations typically consists of several components [27–29]. The volume term is a Woods-Saxon form factor [30] $f(x) = [1 + \exp((x - R)/a)]^{-1}$ with depth V_0 , radius $R = r_0 A^{1/3}$, and diffuseness a . The surface absorption term is proportional to the derivative of the Woods-Saxon form factor, df/dx , and accounts for reactions occurring predominantly at the nuclear surface. The spin-orbit potential couples the intrinsic spin of the projectile to its orbital angular momentum, splitting each $\ell > 0$ partial wave into $j = \ell \pm 1/2$ components. For optical potentials, both the volume and surface terms contain imaginary parts that describe flux loss to non-elastic channels: $V_N = V_{\text{real}} + iW$ with $V_{\text{real}} < 0$ (attractive) and $W < 0$ (absorptive). The Koning-Delaroche parametrization [26] provides energy-dependent values for all these components based on fits to extensive nucleon-nucleus scattering data; similar global parametrizations include the Chapel Hill potential [31].

For scattering states, the asymptotic behavior of the wave function at large x where $V_N(x) \rightarrow 0$ is determined by the Coulomb potential alone. The general solution is a linear combination of incoming and outgoing Coulomb waves,

$$u(x) \xrightarrow{x \rightarrow \infty} A H_\ell^{(-)}(\eta, kx) + B H_\ell^{(+)}(\eta, kx), \quad (2)$$

where $k = \sqrt{2\mu E}/\hbar$ is the wave number, $\eta = Z_1 Z_2 e^2 \mu / (\hbar^2 k)$ is the Sommerfeld parameter characterizing the strength of the Coulomb interaction, and $H_\ell^{(\pm)} = G_\ell \pm iF_\ell$ are the outgoing (+) and incoming (−) Coulomb-Hankel functions constructed from the regular (F_ℓ) and irregular (G_ℓ) Coulomb wave functions [32, 33]. The S-matrix element S_ℓ is defined as the ratio of outgoing to incoming amplitudes, $S_\ell = B/A$, and the phase shift δ_ℓ is

defined through $S_\ell = |S_\ell| e^{2i\delta_\ell}$. For purely elastic scattering with a real potential, $|S_\ell| = 1$ and flux is conserved; absorption reduces $|S_\ell|$ below unity [34, 35].

The traditional approach to solving the scattering problem is to integrate Eq. (1) outward from the origin using methods such as Numerov [36] or Runge-Kutta, imposing the boundary condition $u(0) = 0$ and the correct $r^{\ell+1}$ behavior near the origin. The integration continues to a matching radius r_m sufficiently large that the nuclear potential has decayed to negligible values, typically $r_m \sim 15$ – 20 fm for nucleon-nucleus scattering. At this point, the numerical solution is matched to the known asymptotic form in Eq. (2) to extract S_ℓ . For neutral particles ($\eta = 0$), the Coulomb functions reduce to spherical Bessel functions, while for charged particles, specialized algorithms such as COULCC [33] are required to evaluate them accurately.

This conventional approach, while reliable, does not extend naturally to neural network solvers because of the radiation boundary conditions at large r . Physics-informed neural networks operate on finite computational domains and require boundary conditions that can be specified independently of the solution. Scattering problems, however, require Sommerfeld radiation conditions: the wave function must asymptotically match a superposition of incoming and outgoing waves whose relative amplitude (the S-matrix) is the unknown quantity being computed. These oscillatory conditions cannot be imposed at any finite boundary, and truncating the domain introduces spurious reflections. This fundamental incompatibility has prevented the application of PINNs to scattering problems.

Exterior complex scaling resolves this difficulty by analytically continuing the radial coordinate into the complex plane beyond a scaling radius R_0 [10]. I introduce a smooth coordinate mapping from a parameter coordinate $r \in [0, R_{\text{max}}]$ (always real) to a physical coordinate $x(r)$ that becomes complex for $r > R_0$. The mapping is constructed using a smooth switching function

$$s(t) = \begin{cases} 0 & t \leq 0 \\ 3t^2 - 2t^3 & 0 < t < 1, \\ 1 & t \geq 1 \end{cases}, \quad t = \frac{r - R_0}{w}, \quad (3)$$

where w is the width of the transition region, typically chosen as $w \approx 0.1R_0$ to ensure a smooth but localized transition. This polynomial form ensures that $s(t)$ and its first derivative are continuous everywhere, avoiding discontinuities that could cause numerical difficulties. The physical coordinate is then

$$x(r) = r + (e^{i\theta} - 1)I(r), \quad (4)$$

where θ is the rotation angle and $I(r)$ is the integral of the switching function,

$$I(r) = \int_0^r s\left(\frac{r' - R_0}{w}\right) dr'. \quad (5)$$

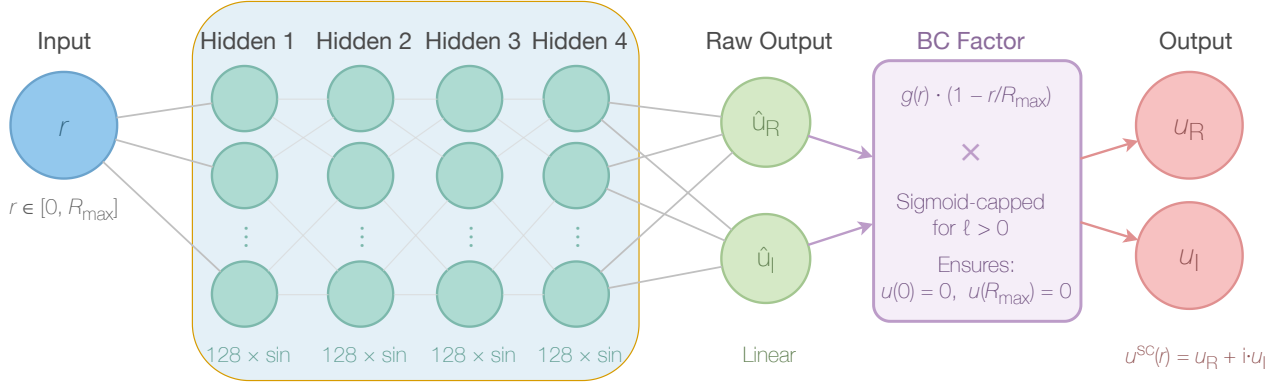


FIG. 1. Neural network architecture for PINN-ECS. The network takes the radial coordinate r as input and passes it through four hidden layers of 128 neurons each with sinusoidal activation functions. The raw network output $\hat{u}(r)$ is multiplied by the boundary condition factor $g(r) = r^{\ell+1}(1 - r/R_{\max})\sigma_c(r)$, where the sigmoid cap $\sigma_c(r)$ prevents numerical overflow for high angular momentum channels. This hard-coded construction ensures $u(0) = u(R_{\max}) = 0$ exactly, regardless of the learned weights.

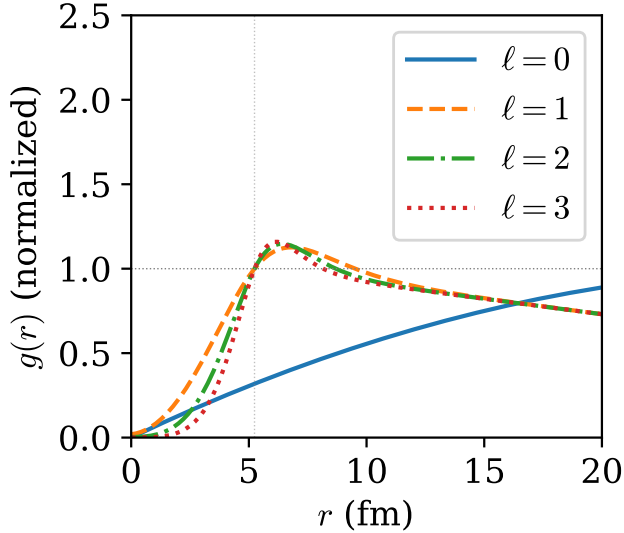


FIG. 2. Normalized boundary condition factor $g(r)$ showing the sigmoid capping that prevents growth beyond $R_{\text{nuc}}^{\ell+1}$: $\ell = 0$ (solid), $\ell = 1$ (dashed), $\ell = 2$ (dash-dotted), and $\ell = 3$ (dotted). The vertical dashed line marks R_{nuc} . For $\ell > 0$, the factor transitions smoothly from $r^{\ell+1}$ behavior near the origin to a bounded value $R_{\text{nuc}}^{\ell+1}$ in the asymptotic region.

This integral has a closed-form expression: $I(r) = 0$ for $r \leq R_0$, $I(r) = w(t^3 - t^4/2)$ for $R_0 < r < R_0 + w$, and $I(r) = w/2 + (r - R_0 - w)$ for $r \geq R_0 + w$. The Jacobian of the transformation is

$$q(r) = \frac{dx}{dr} = 1 + (e^{i\theta} - 1) s \left(\frac{r - R_0}{w} \right), \quad (6)$$

which equals unity for $r \leq R_0$ (where $x = r$ is real) and approaches $e^{i\theta}$ for $r \geq R_0 + w$ (where x increases along a ray at angle θ in the complex plane).

The effect of this coordinate transformation on outgoing waves is crucial. An outgoing wave e^{ikx} in the ECS region becomes $e^{ikx(r)} = e^{ik[r \cos \theta + iy(r)]}$, where $y(r) = \text{Im}[x(r)]$ increases approximately as $(r - R_0) \sin \theta$ for $r > R_0 + w$. The amplitude therefore decays as $e^{-k(r - R_0) \sin \theta}$, converting the oscillatory wave into an exponentially damped function. For the ECS absorbing boundary to work effectively, this decay must be sufficient to suppress the wave function at the outer boundary $r = R_{\max}$. The decay factor is $\exp[-k(R_{\max} - R_0) \sin \theta]$, and I require this to be less than approximately 10^{-3} for adequate absorption. With typical parameters $\theta = 12^\circ$, $R_0 = 20$ fm, and $R_{\max} = 60$ fm, the decay factor for $n+^{40}\text{Ca}$ at 20 MeV ($k \approx 0.95 \text{ fm}^{-1}$) is about 4×10^{-4} , ensuring greater than 99.9% absorption.

Unlike uniform complex scaling where the nuclear potential must be evaluated at complex coordinates, ECS keeps the nuclear interaction region on the real axis by choosing R_0 beyond the range of V_N . This avoids singularities in the Woods-Saxon form factor that would otherwise restrict the rotation angle. The choice $\theta = 12^\circ$ provides adequate absorption while maintaining numerical stability.

Under the ECS coordinate transformation, the differential operators transform according to the chain rule. The first derivative becomes $d/dx = q^{-1} d/dr$, and the second derivative is

$$\frac{d^2}{dx^2} = \frac{1}{q^2} \frac{d^2}{dr^2} - \frac{q'}{q^3} \frac{d}{dr}, \quad (7)$$

where $q' = dq/dr = (e^{i\theta} - 1)(6t - 6t^2)/w$ in the transition region $0 < t < 1$, and $q' = 0$ outside this region. The transformed Schrödinger equation in the parameter coordinate r takes the form

$$-\frac{\hbar^2}{2\mu} \left(\frac{1}{q^2} u'' - \frac{q'}{q^3} u' \right) + \frac{\hbar^2 \ell(\ell + 1)}{2\mu x(r)^2} u + V(x(r)) u = E u, \quad (8)$$

where primes denote derivatives with respect to r and $V(x) = V_N(x) + V_C(x)$ is the total potential. The critical simplification is that for $r > R_0$, I set $V_N = 0$ because the nuclear potential has negligible range beyond the nuclear surface. Only the Coulomb potential requires evaluation at complex coordinates, and this is straightforward since $1/x$ is analytic everywhere except at the origin.

For the scattering problem, I employ a driven-equation formulation that separates the total wave function into incident and scattered components,

$$u(r) = u^{\text{in}}(r) + u^{\text{sc}}(r), \quad (9)$$

where $u^{\text{in}}(r) = F_\ell(\eta, kx(r))$ is the regular Coulomb wave function representing the incident flux, computed with the point-Coulomb Sommerfeld parameter η . The scattered wave $u^{\text{sc}}(r)$ satisfies the inhomogeneous driven equation

$$(H - E) u^{\text{sc}}(r) = -V_{\text{short}}(r) u^{\text{in}}(r), \quad (10)$$

where H is the Hamiltonian operator including kinetic energy, centrifugal barrier, the charged-sphere Coulomb potential, and the nuclear optical potential. The short-range potential $V_{\text{short}} = V_N + (V_C^{\text{sphere}} - V_C^{\text{point}})$ includes both the nuclear potential and the charged-sphere correction; the latter arises because the incident Coulomb wave is a solution of the point-Coulomb Schrödinger equation, not the charged-sphere equation. The key observation is that V_{short} vanishes for r beyond both the nuclear radius and the Coulomb radius R_C . This means the right-hand side of Eq. (10) is confined entirely to the real-axis region $r \leq R_0$, and no analytic continuation of V_{short} is required. In the ECS region, the scattered wave satisfies the homogeneous equation $(H - E)u^{\text{sc}} = 0$ with exponentially decaying boundary conditions, which is precisely the type of problem that neural networks can solve efficiently.

The S-matrix element is extracted by matching the total wave function to its asymptotic form at a matching radius $r_m < R_0$ (on the real axis). The matching conditions involve the Wronskians of the wave function with the Coulomb functions. I compute the quantities

$$N = kuF'_\ell - u'F_\ell, \quad (11)$$

$$D = u'G'_\ell - kuG'_\ell, \quad (12)$$

where all functions are evaluated at $r = r_m$ and derivatives are with respect to the dimensionless variable $\rho = kr$. The K-matrix $K = \tan \delta_\ell = N/D$ gives the phase shift, but this formula fails when $D \rightarrow 0$ (corresponding to $\delta_\ell \rightarrow \pm 90^\circ$). I instead compute the S-matrix directly as

$$S_\ell = \frac{D + iN}{D - iN}, \quad (13)$$

which is well-defined for all phase shifts. The phase shift is then $\delta_\ell = \arg(S_\ell)/2$ and the absorption is characterized by $|S_\ell| \leq 1$. To improve robustness, I average the S-matrix over five matching radii distributed uniformly in the interval $[0.7R_0, 0.9R_0]$, which reduces sensitivity to local fluctuations in the numerical solution.

III. COMPUTATIONAL METHOD

The PINN-ECS method combines exterior complex scaling, which transforms oscillatory scattering waves into decaying functions, with a physics-informed neural network that learns the scattered wave function by minimizing the differential equation residual. The key components include the ECS coordinate mapping, the network architecture with hard-coded boundary conditions, and the driven-equation formulation that confines the nuclear potential to the real axis.

The physics-informed neural network represents the scattered wave function $u^{\text{sc}}(r)$ as a parameterized function of the radial coordinate. The network architecture consists of a fully-connected feedforward network with $r \in [0, R_{\text{max}}]$ as input and two outputs representing the real and imaginary parts of the complex wave function, $u_R(r)$ and $u_I(r)$. I use four hidden layers with 128 neurons each and sinusoidal activation functions, $\sigma(z) = \sin(z)$, which are particularly well-suited for representing oscillatory solutions [37, 38]. The raw network output $\hat{u}(r)$ is then modified to enforce boundary conditions exactly.

The boundary conditions $u^{\text{sc}}(0) = 0$ and $u^{\text{sc}}(R_{\text{max}}) = 0$ are enforced through a multiplicative factor,

$$u^{\text{sc}}(r) = \frac{g(r)(1 - r/R_{\text{max}})}{\mathcal{N}} \hat{u}(r), \quad (14)$$

where \mathcal{N} is a normalization constant and $g(r)$ encodes the correct $r^{\ell+1}$ behavior near the origin. A naive choice $g(r) = r^{\ell+1}$ becomes problematic at high angular momentum. Since the final wave function is the product $u^{\text{sc}} \propto g(r) \cdot \hat{u}(r)$ and must remain bounded, a large $g(r)$ requires the network to output proportionally small values of $\hat{u}(r)$. For example, at $\ell = 5$ and $r = R_0 = 20$ fm, the factor $r^{\ell+1} \approx 6 \times 10^7$. To produce a bounded wave function, the optimizer must drive all network weights toward small values, which compresses the dynamic range available for representing the detailed structure in the nuclear interior.

I resolve this problem with a sigmoid-capped boundary condition factor,

$$g(r) = (1 - \sigma_c) r^{\ell+1} + \sigma_c R_{\text{nuc}}^{\ell+1}, \quad (15)$$

where R_{nuc} is a characteristic nuclear radius (I use $R_{\text{nuc}} = 1.25A^{1/3}$ fm) and σ_c is a smooth transition function,

$$\sigma_c(r) = \left[1 + \exp \left(-\frac{2(\ell+1)}{R_{\text{nuc}}} (r - R_{\text{nuc}}) \right) \right]^{-1}. \quad (16)$$

This construction ensures that $g(r) \approx r^{\ell+1}$ for $r \ll R_{\text{nuc}}$ (preserving the correct behavior at the origin) while $g(r) \rightarrow R_{\text{nuc}}^{\ell+1}$ for $r \gg R_{\text{nuc}}$ (bounded in the asymptotic region). Figure 1 shows how this BC factor is integrated into the neural network architecture, where the raw network output is multiplied by $g(r)$ to enforce the

boundary conditions exactly. Figure 2 illustrates how this capping prevents the pathological growth for high- ℓ channels. The normalized BC factor $g(r)$ is shown for $\ell = 0$ (solid), $\ell = 1$ (dashed), $\ell = 2$ (dash-dotted), and $\ell = 3$ (dotted). The vertical dashed line marks R_{nuc} . For $\ell > 0$, the factor rises steeply near the origin following $r^{\ell+1}$, then saturates to a constant beyond R_{nuc} . For $\ell = 0$, where the uncapped factor $r(1 - r/R_{\text{max}})$ is already well-behaved, I skip the sigmoid capping.

The loss function combines the differential equation residual with an anchor term that prevents the trivial solution $u^{\text{sc}} = 0$. The residual loss is

$$\mathcal{L}_{\text{res}} = \frac{1}{N_c} \sum_{i=1}^{N_c} |[(H - E)u^{\text{sc}} + V_{\text{short}}u^{\text{in}}](r_i)|^2, \quad (17)$$

where the sum runs over N_c collocation points $\{r_i\}$ and the Hamiltonian action is computed using automatic differentiation [39] for the scattered wave derivatives. The anchor loss prevents the optimizer from finding the trivial solution $u^{\text{sc}} = 0$,

$$\mathcal{L}_{\text{anchor}} = w_a \exp\left(-\frac{\langle |u^{\text{sc}}|^2 \rangle}{s_a}\right), \quad (18)$$

where $\langle \cdot \rangle$ denotes the mean over collocation points, w_a is the anchor weight, and s_a is a scale parameter. When $u^{\text{sc}} \approx 0$, the exponential approaches unity and the loss receives a penalty of w_a ; when $|u^{\text{sc}}|^2 \gg s_a$, the anchor loss vanishes and does not interfere with residual minimization. The total loss is $\mathcal{L} = \mathcal{L}_{\text{res}} + \mathcal{L}_{\text{anchor}}$. The scale parameter is set automatically based on the source term magnitude,

$$s_a = \max(\langle |V_{\text{short}}F_\ell|^2 \rangle, 0.1), \quad (19)$$

which ensures that the anchor contribution remains comparable to the residual across all partial waves, eliminating the need for manual tuning. The minimum value of 0.1 prevents the anchor from becoming too weak for high- ℓ channels where the source term is small due to the centrifugal barrier.

The collocation points are distributed non-uniformly to concentrate sampling in regions of rapid variation. I allocate 50% of the points to the nuclear interior $r \in [0, 2R_{\text{nuc}}]$, 20% to the intermediate region $r \in [2R_{\text{nuc}}, R_0]$, and 30% to the ECS region $r \in [R_0, R_{\text{max}}]$. Within each region, points are drawn from a uniform distribution. All computations are performed in double precision (float64) to ensure accurate phase shift extraction.

Training proceeds in two stages. The first stage uses the Adam optimizer [40] with learning rate 5×10^{-4} and cosine annealing, where each epoch consists of one gradient descent step using all collocation points. Adam is robust to the choice of initial learning rate and handles the ill-conditioning of the loss landscape gracefully [41]. The second stage switches to L-BFGS [42] with strong Wolfe line search, where each epoch performs one quasi-Newton

update with up to 20 line search evaluations. L-BFGS provides quadratic convergence near the minimum and refines the solution to high accuracy. Network weights are initialized with a fixed random seed (42) to ensure reproducibility. The implementation uses PyTorch [43] for automatic differentiation and GPU acceleration. The specific training parameters vary by system: for n+ ^{40}Ca , I use 2000 collocation points, 20,000 Adam epochs, and 800 L-BFGS epochs; for $^{6}\text{Li}+^{208}\text{Pb}$, I use 4000 collocation points, 30,000 Adam epochs, and 1000 L-BFGS epochs to accommodate the stronger Coulomb interaction and larger number of partial waves.

For heavy-ion systems with strong Coulomb barriers, I employ a causal training strategy [44] that builds the solution from the nuclear interior outward. The source term $V_N F_\ell$ in the driven equation is localized within the nuclear radius, so the scattered wave originates from this region and propagates outward. Training all radii simultaneously can lead to spurious solutions in the outer region where the source term vanishes. To avoid this, I progressively expand the training region from R_{nuc} to R_0 over N_{warmup} epochs (typically 3000):

$$L(n) = R_{\text{nuc}} + (R_0 - R_{\text{nuc}}) \cdot \min(n/N_{\text{warmup}}, 1), \quad (20)$$

where $L(n)$ is the outer boundary of the training region at epoch n . Points beyond $L(n)$ contribute less to the loss, ensuring that the interior solution is established before fitting the asymptotic region.

IV. RESULTS

I validate the PINN-ECS method on two benchmark systems that test different aspects of the approach: nucleon-nucleus scattering with a full optical potential, and heavy-ion scattering with strong Coulomb effects.

The first benchmark is neutron scattering on ^{40}Ca at $E_{\text{lab}} = 20$ MeV, a well-studied system with extensive experimental data and established optical potentials. I use the Koning-Delaroche (KD02) global optical potential [26], which includes real and imaginary volume terms, a surface absorption term, and a spin-orbit potential. The spin-orbit interaction splits each $\ell > 0$ partial wave into $j = \ell + 1/2$ and $j = \ell - 1/2$ components with different phase shifts. I compute 21 channels in total, corresponding to $\ell = 0$ through $\ell = 10$: $s_{1/2}$ for $\ell = 0$, and both $j = \ell \pm 1/2$ spin-orbit partners for $\ell = 1-10$. The ECS parameters are $R_0 = 20$ fm, $R_{\text{max}} = 60$ fm, $\theta = 12^\circ$, and the transition width is $w = 0.1R_0 = 2$ fm.

Figure 3 compares PINN-ECS results with reference values from the COLOSS code [18], which solves the same scattering problem using conventional complex scaling with Lagrange-mesh discretization. Panel (a) shows the phase shifts δ for all 21 channels, where black squares connected by lines represent the COLOSS reference and red circles show the PINN-ECS results. The two methods agree so well that the symbols overlap for most channels. Panel (b) displays the S-matrix magnitudes $|S|$, which

TABLE I. Phase shifts and S-matrix elements for $n+^{40}\text{Ca}$ at $E_{\text{lab}} = 20$ MeV. Selected channels are shown comparing PINN-ECS to the COLOSS reference.

Channel	δ_{PINN}	δ_{COL}	$\Delta\delta$	$ S _{\text{PINN}}$	$ S _{\text{COL}}$
$s_{1/2}$	+16.24°	+16.27°	-0.03°	0.415	0.415
$p_{3/2}$	+11.05°	+11.10°	-0.05°	0.518	0.518
$d_{5/2}$	+6.18°	+6.19°	-0.01°	0.402	0.401
$f_{5/2}$	-46.85°	-46.85°	+0.00°	0.497	0.497
$g_{9/2}$	-35.70°	-35.66°	-0.04°	0.537	0.537
$h_{11/2}$	+8.62°	+8.46°	+0.16°	0.227	0.230

characterize absorption into non-elastic channels. The horizontal dashed line marks the unitarity limit $|S| = 1$. Panel (c) shows the phase shift errors $\Delta\delta = \delta_{\text{PINN}} - \delta_{\text{COLOSS}}$ as a bar chart. For low- ℓ channels ($\ell \leq 5$), the errors are below 0.1° . For the highest partial waves ($\ell = 6-10$), the errors increase but remain below 1.5° in all cases.

Table I presents a quantitative comparison for selected channels. The $s_{1/2}$ wave shows $\delta_{\text{PINN}} = 16.24^\circ$ compared to $\delta_{\text{COLOSS}} = 16.27^\circ$, an error of only 0.03° . The $f_{5/2}$ wave, with a large negative phase shift of -46.85° , is reproduced exactly. The most challenging channel is $j_{15/2}$ with $\ell = 7$ and very small phase shift ($\sim 1^\circ$), where the relative error is larger but the absolute accuracy remains adequate for most applications. The consistency of $|S|$ values between the two methods confirms that the imaginary part of the optical potential, which describes absorption, is correctly handled by the PINN-ECS approach.

The auto-adaptive anchor mechanism plays a crucial role in achieving consistent accuracy across partial waves. Figure 4 shows how the anchor scale decreases with angular momentum due to centrifugal suppression of the source term $V_N F_\ell$. The scale drops by over three orders of magnitude from $\ell = 0$ to $\ell = 6$, after which the minimum floor of 0.1 is applied. This automatic adaptation ensures that the anchor contribution remains comparable to the residual loss across all partial waves, eliminating the need for manual tuning.

The second benchmark is $^6\text{Li}+^{208}\text{Pb}$ elastic scattering at $E_{\text{lab}} = 40$ MeV, a heavy-ion system with strong Coulomb effects. The Sommerfeld parameter $\eta = Z_1 Z_2 e^2 \mu / (\hbar^2 k) \approx 15$ indicates that multiple Coulomb scattering events occur before the nuclear interaction, creating a thick Coulomb barrier that strongly modifies the scattering pattern. I compute 41 partial waves from $\ell = 0$ to $\ell = 40$ to capture the complete angular distribution. The optical potential includes a Woods-Saxon nuclear term with parameters fitted to this mass region, and the Coulomb potential is that of a uniformly charged sphere with radius $R_C \approx 7.7$ fm. The ECS parameters are $R_0 = 20$ fm, $R_{\text{max}} = 50$ fm, and $\theta = 12^\circ$. For this heavy-ion system, I employ the causal training strategy with $N_{\text{warmup}} = 3000$ epochs to ensure stable convergence

TABLE II. S-matrix elements for $^6\text{Li}+^{208}\text{Pb}$ at $E_{\text{lab}} = 40$ MeV. Selected partial waves are shown comparing PINN-ECS to the COLOSS reference.

ℓ	$\text{Re } S_{\text{PINN}}$	$\text{Re } S_{\text{COL}}$	$\text{Im } S_{\text{PINN}}$	$\text{Im } S_{\text{COL}}$	$\Delta S $
0	-0.014	-0.014	-0.007	-0.006	+0.001
5	-0.012	-0.011	-0.019	-0.019	+0.000
10	+0.040	+0.039	-0.041	-0.042	+0.000
15	+0.237	+0.237	+0.036	+0.037	+0.000
20	+0.687	+0.684	+0.128	+0.130	+0.002
25	+0.943	+0.925	+0.028	+0.044	+0.017
30	+0.996	+0.983	+0.001	+0.009	+0.013
40	+1.000	+0.999	-0.001	+0.000	+0.001

across all partial waves.

Figure 5 presents the results for the $^6\text{Li}+^{208}\text{Pb}$ system. Panel (b) shows the S-matrix magnitudes, which exhibit the characteristic pattern of heavy-ion scattering: strong absorption ($|S| \ll 1$) at low angular momenta where the trajectories penetrate inside the Coulomb barrier, a transition region around $\ell \sim 15-25$ corresponding to grazing collisions, and transparency ($|S| \rightarrow 1$) at high angular momenta where the centrifugal barrier prevents nuclear contact. Panel (a) shows the Rutherford ratio, which exhibits oscillations arising from interference between the Coulomb and nuclear scattering amplitudes, a signature feature of heavy-ion scattering near the Coulomb barrier. The PINN-ECS results (dashed line and circles) agree well with the COLOSS reference (solid line) for both observables.

Table II presents a quantitative comparison of S-matrix elements for selected partial waves spanning the absorption-to-transparency transition. The agreement between PINN-ECS and COLOSS is excellent for most channels, with $|S|$ differences below 0.01 in the absorption region ($\ell \lesssim 20$). Slightly larger discrepancies appear at high- ℓ ($\Delta|S| \sim 0.01-0.02$ for $\ell = 25-30$), corresponding to the late transition region where $|S| \rightarrow 1$; these errors have minimal impact on the angular distribution because the nuclear scattering amplitude is proportional to $(S_\ell - 1)$, which vanishes as $|S| \rightarrow 1$.

The angular distribution is computed from the S-matrix elements using the standard partial-wave expansion,

$$\frac{d\sigma/d\Omega}{(d\sigma/d\Omega)_{\text{Ruth}}} = \frac{|f_C(\theta) + f_N(\theta)|^2}{|f_C(\theta)|^2}, \quad (21)$$

where $f_C(\theta)$ is the pure Coulomb scattering amplitude and $f_N(\theta)$ is the nuclear contribution arising from deviations of S_ℓ from unity. The Coulomb amplitude includes the characteristic $1/\sin^2(\theta/2)$ divergence and a phase factor involving the Coulomb phase shifts $\sigma_\ell = \arg \Gamma(\ell + 1 + i\eta)$. The sum over partial waves in f_N converges slowly for heavy-ion systems because many angular momenta contribute, but with 41 partial waves the angular distribution is well-converged at all angles shown.

Figure 6 illustrates the training dynamics for the $n+^{40}\text{Ca}$ benchmark. Channels are trained sequentially, with transfer learning applied within each ℓ value (from $j = \ell - 1/2$ to $j = \ell + 1/2$). The loss decreases rapidly during training, dropping by several orders of magnitude. Notably, the $s_{1/2}$ channel converges to a relatively high loss (~ 0.8) compared to other channels (~ 0.1), yet still produces accurate phase shifts and S-matrix elements (see Fig. 3). This demonstrates the robustness of the PINN-ECS method: the physical observables are insensitive to the precise value of the training loss once the solution has captured the essential features of the wave function. Each partial wave requires approximately 10–15 minutes on a single NVIDIA RTX 3090 GPU.

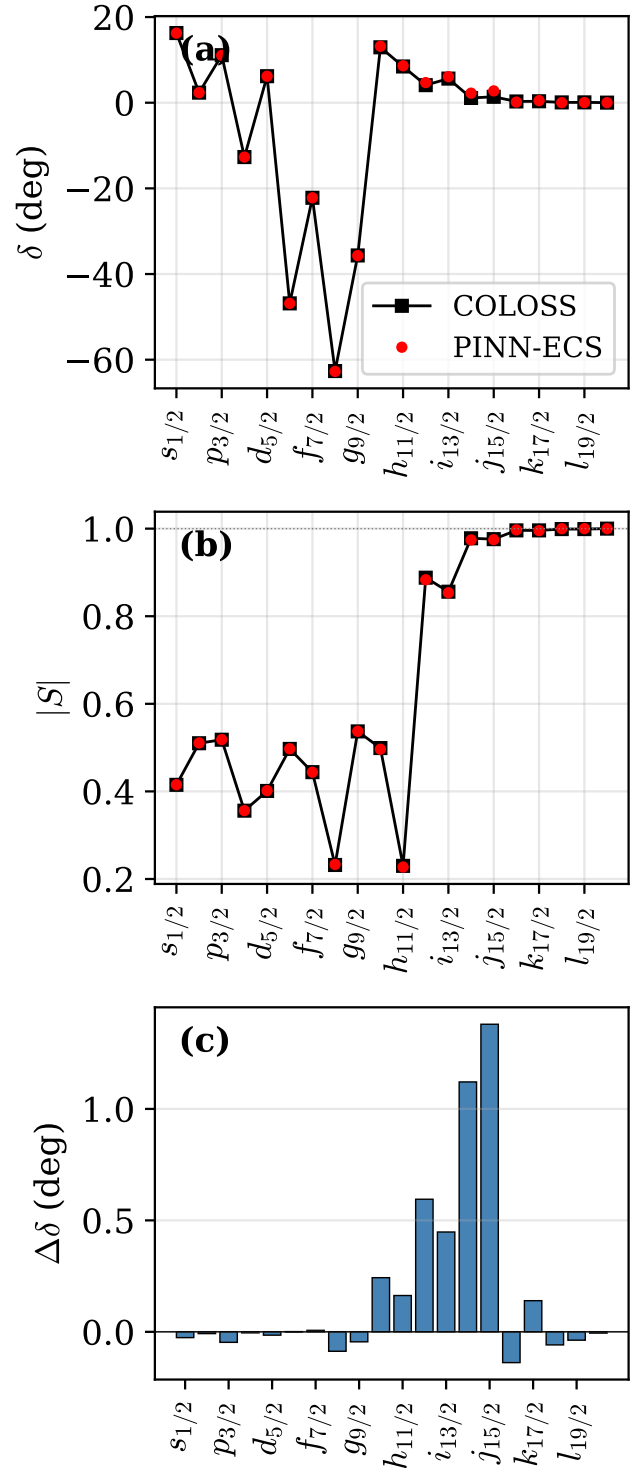


FIG. 3. PINN-ECS results for $n+^{40}\text{Ca}$ scattering at $E_{\text{lab}} = 20$ MeV with the KD02 optical potential. (a) Phase shifts δ comparing PINN-ECS (circles) to COLOSS reference (squares). (b) S-matrix magnitudes $|S|$. (c) Phase shift errors $\Delta\delta = \delta_{\text{PINN}} - \delta_{\text{COLOSS}}$.

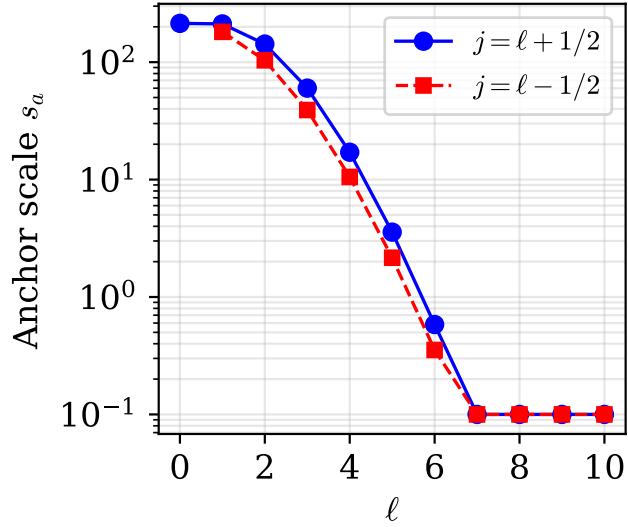


FIG. 4. Auto-adaptive anchor scale s_a versus angular momentum ℓ for $n+^{40}\text{Ca}$. The scale is computed from $s_a = \max(\langle |V_{\text{short}} F_\ell|^2 \rangle, 0.1)$ and decreases with ℓ due to centrifugal suppression of the source term. Circles with solid line: $j = \ell + 1/2$; squares with dashed line: $j = \ell - 1/2$. The floor value of 0.1 is applied for $\ell \geq 7$.

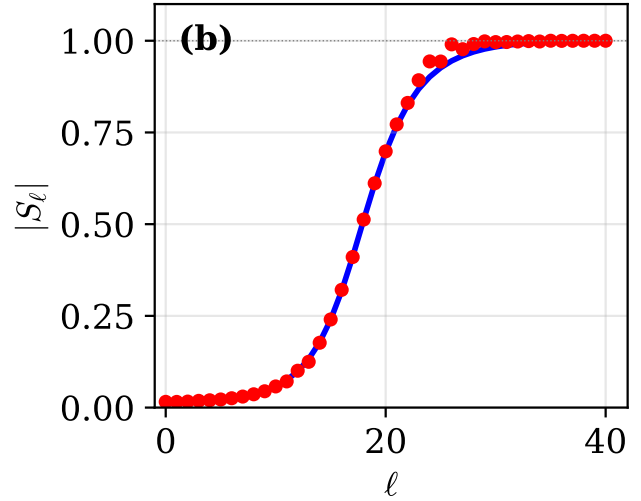
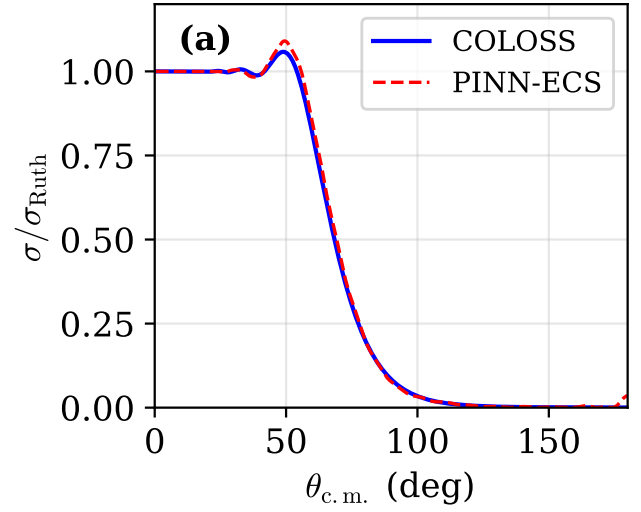


FIG. 5. ${}^6\text{Li}+{}^{208}\text{Pb}$ elastic scattering at $E_{\text{lab}} = 40$ MeV. (a) Rutherford ratio versus center-of-mass angle: COLOSS (solid line) and PINN-ECS (dashed line). (b) S-matrix magnitude $|S_\ell|$ versus partial wave ℓ : COLOSS (solid line) and PINN-ECS (circles). The horizontal dashed line marks the unitarity limit $|S| = 1$.

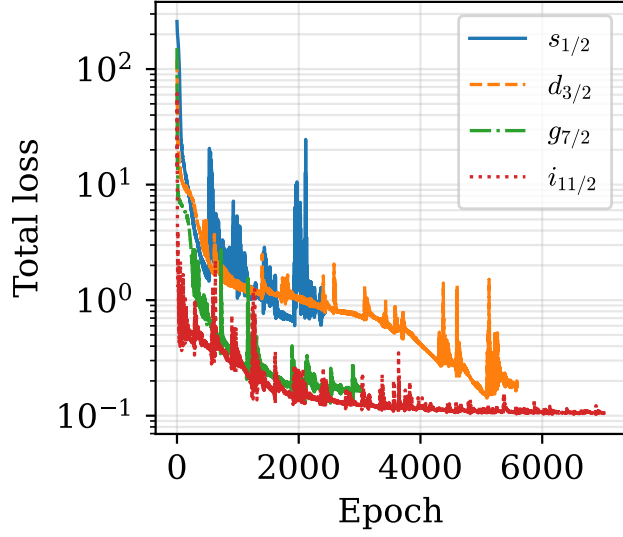


FIG. 6. Training convergence for $n+^{40}\text{Ca}$ scattering. Four representative channels are shown: $s_{1/2}$ (solid), $d_{3/2}$ (dashed), $g_{7/2}$ (dash-dotted), and $i_{11/2}$ (dotted). Higher- ℓ channels exhibit lower initial loss due to centrifugal suppression of the source term. Notably, $s_{1/2}$ converges to a relatively high loss (~ 0.8) yet still yields accurate phase shifts (see Fig. 3), demonstrating the method's robustness.

V. DISCUSSION

The results presented above demonstrate that the combination of exterior complex scaling with physics-informed neural networks provides an accurate and reliable method for solving nuclear scattering problems. The key enabling insight is that ECS transforms the oscillatory scattering boundary conditions into decaying waves that neural networks can represent naturally, while the driven-equation formulation confines the nuclear potential to the real axis where it is well-defined. Several aspects of the method merit further discussion.

It is important to emphasize that the ECS transformation itself is well-established methodology with decades of development in atomic and molecular physics [10, 13, 16]. The choice of ECS parameters (R_0 , θ , R_{\max}) follows standard criteria: the scaling radius R_0 must exceed the range of nuclear forces, the rotation angle θ must be small enough to avoid singularities in the Woods-Saxon potential (typically $\theta \lesssim 15^\circ$), and the outer boundary R_{\max} must be large enough to ensure adequate absorption of outgoing waves. These constraints are intrinsic to complex scaling and apply equally to any discretization method, whether finite differences, R-matrix, or neural networks. The present work does not aim to improve ECS itself, but rather to demonstrate that PINNs can serve as an effective solver within the ECS framework, thereby inheriting the advantages of neural networks (differentiability, mesh-free formulation) while leveraging the boundary condition transformation that ECS provides.

The accuracy achieved for nucleon-nucleus scattering, with phase shift errors below 0.1° for most partial waves, is comparable to that of established numerical methods such as Numerov integration [36] or R-matrix theory [20]. The slightly larger errors observed for the highest partial waves ($\ell \geq 6$) arise from the combination of weak source terms and the sensitivity of small phase shifts to numerical noise. For applications where high- ℓ accuracy is critical, such as analyzing forward-angle scattering data, additional collocation points or extended training may be beneficial. However, for typical optical-model analyses where low and intermediate partial waves dominate the cross section, the present accuracy is more than adequate.

The driven-equation approach has a significant advantage over directly solving for the total wave function: it naturally separates the known asymptotic behavior (encoded in the incident Coulomb wave) from the unknown scattered contribution. This separation means the neural network only needs to represent the relatively smooth scattered wave rather than the rapidly oscillating total wave function, which simplifies the learning task. Furthermore, the source term $V_{\text{short}}F_\ell$ provides an automatic scale for the solution magnitude, reducing the ambiguity inherent in homogeneous eigenvalue problems.

The primary motivation for developing PINN-based scattering solvers is not to replace efficient conventional methods for single-channel problems, but to establish a foundation for applications where the differentiable,

mesh-free nature of neural networks offers distinct advantages [45]. For inverse problems, such as fitting optical potential parameters to experimental cross sections, the end-to-end differentiability of the PINN framework enables gradient-based optimization without requiring expensive outer-loop optimization over repeated forward solves. For coupled-channel reactions involving particle transfer or inelastic excitation [46–48], multi-output neural networks can represent coupled wave functions without explicitly constructing and solving large matrix equations. For few-body scattering (e.g., three-body Faddeev equations [24, 49, 50]), the mesh-free nature of PINNs may help mitigate the exponential scaling of grid-based methods with dimensionality.

The computational cost of the PINN-ECS method is dominated by the training iterations required for each partial wave. With current hardware and hyperparameters, each channel requires approximately 10–15 minutes on a single NVIDIA RTX 3090 GPU. For a complete calculation with 20–40 partial waves, the total wall-clock time is on the order of several hours, which is significantly longer than conventional integration methods (which require seconds per partial wave) but acceptable for research applications where end-to-end differentiability or mesh-free formulations are required. The training time could likely be reduced by using smaller networks for simple potentials or by warm-starting from nearby energies [51, 52].

VI. CONCLUSIONS

I have demonstrated that exterior complex scaling enables physics-informed neural networks to solve quantum scattering problems in nuclear physics. The key innovation is using ECS to transform oscillatory scattering boundary conditions into exponentially decaying waves that neural networks can represent naturally, combined with a driven-equation formulation that confines nuclear potentials to the real axis. The method has been validated on nucleon-nucleus scattering ($n+^{40}\text{Ca}$ at 20 MeV) achieving phase shift accuracy of $\Delta\delta < 0.1^\circ$ for most partial waves, and on heavy-ion scattering ($^6\text{Li}+^{208}\text{Pb}$ at 40 MeV) demonstrating correct Coulomb-nuclear interference patterns.

Several technical innovations contribute to the reliability of the method: the sigmoid-capped boundary condition factor prevents high- ℓ pathologies by limiting the growth of the angular momentum prefactor; the auto-adaptive anchor mechanism balances the residual and normalization losses across all partial waves; and the two-stage training protocol (Adam followed by L-BFGS) provides both robust initial convergence and high final accuracy. The extraction of phase shifts using automatic differentiation and multi-point S-matrix averaging ensures that derivatives are computed accurately without numerical finite-difference errors.

The PINN-ECS approach opens several directions for

future research. The most immediate application is inverse problems: fitting optical potential parameters directly to experimental elastic scattering data by exploiting the end-to-end differentiability of the computational pipeline. Coupled-channels calculations for reactions involving particle transfer or nuclear excitation could be addressed by representing multiple channel wave functions with a multi-output network, avoiding the need to explicitly construct coupled integro-differential equations. Extension to few-body scattering problems [25, 53], where the mesh-free nature of neural networks may help mitigate the curse of dimensionality faced by grid-based methods, represents a longer-term goal.

More broadly, this work demonstrates that the combination of physics-informed machine learning with analytic transformations such as complex scaling can extend

the reach of neural network methods to problems that appear intractable within the standard PINN framework. The philosophy of transforming a difficult PINN problem into one that matches the inductive biases of neural networks, namely smooth, bounded, decaying solutions, may prove fruitful in other areas of computational physics where boundary conditions pose fundamental challenges.

ACKNOWLEDGMENTS

This work was supported by the National Natural Science Foundation of China (Grant Nos. 12475132 and 12535009) and the Fundamental Research Funds for the Central Universities.

-
- [1] P. Fröbrich and R. Lipperheide, *Theory of Nuclear Reactions* (Oxford University Press, 1996).
- [2] I. J. Thompson and F. M. Nunes, *Nuclear Reactions for Astrophysics* (Cambridge University Press, 2009).
- [3] I. E. Lagaris, A. Likas, and D. I. Fotiadis, *IEEE Trans. Neural Netw.* **9**, 987 (1998).
- [4] M. Raissi, P. Perdikaris, and G. E. Karniadakis, *J. Comput. Phys.* **378**, 686 (2019).
- [5] G. E. Karniadakis, I. G. Kevrekidis, L. Lu, P. Perdikaris, S. Wang, and L. Yang, *Nat. Rev. Phys.* **3**, 422 (2021).
- [6] G. Carleo and M. Troyer, *Science* **355**, 602 (2017).
- [7] J. Hermann, Z. Schätzle, and F. Noé, *Nat. Chem.* **12**, 891 (2020).
- [8] D. Pfau, J. S. Spencer, A. G. D. G. Matthews, and W. M. C. Foulkes, *Phys. Rev. Res.* **2**, 033429 (2020).
- [9] L. Lu, X. Meng, Z. Mao, and G. E. Karniadakis, *SIAM Rev.* **63**, 208 (2021).
- [10] B. Simon, *Phys. Lett. A* **71**, 211 (1979).
- [11] W. P. Reinhardt, *Annu. Rev. Phys. Chem.* **33**, 223 (1982).
- [12] Y. K. Ho, *Phys. Rep.* **99**, 1 (1983).
- [13] N. Moiseyev, *Phys. Rep.* **302**, 212 (1998).
- [14] J.-P. Berenger, *J. Comput. Phys.* **114**, 185 (1994).
- [15] X. Antoine and E. Lorin, *Mol. Phys.* **115**, 1861 (2017).
- [16] T. N. Rescigno and C. W. McCurdy, *Phys. Rev. A* **62**, 032706 (2000).
- [17] T. Myo, Y. Kikuchi, H. Masui, and K. Katō, *Prog. Theor. Exp. Phys.* **2020**, 12A101 (2020).
- [18] J. Liu, J. Lei, and Z. Ren, *Comput. Phys. Commun.* **311**, 109568 (2025).
- [19] E. P. Wigner and L. Eisenbud, *Phys. Rev.* **72**, 29 (1947).
- [20] A. M. Lane and R. G. Thomas, *Rev. Mod. Phys.* **30**, 257 (1958).
- [21] P. Descouvemont and D. Baye, *Rep. Prog. Phys.* **73**, 036301 (2010).
- [22] A. E. Thorlacius and E. D. Cooper, *J. Comput. Phys.* **72**, 70 (1987).
- [23] L. D. Faddeev, *Sov. Phys. JETP* **12**, 1014 (1961), [*Zh. Eksp. Teor. Fiz.* 39, 1459 (1960)].
- [24] L. D. Faddeev and S. P. Merkuriev, *Quantum Scattering Theory for Several Particle Systems* (Springer, 1993).
- [25] R. Lazauskas and J. Carbonell, *Front. Phys.* **7**, 251 (2019).
- [26] A. J. Koning and J. P. Delaroche, *Nucl. Phys. A* **713**, 231 (2003).
- [27] H. Feshbach, *Ann. Phys.* **5**, 357 (1958).
- [28] H. Feshbach, *Ann. Phys.* **19**, 287 (1962).
- [29] G. R. Satchler, *Direct Nuclear Reactions* (Oxford University Press, 1983).
- [30] R. D. Woods and D. S. Saxon, *Phys. Rev.* **95**, 577 (1954).
- [31] R. L. Varner, W. J. Thompson, T. L. McAbee, E. J. Ludwig, and T. B. Clegg, *Phys. Rep.* **201**, 57 (1991).
- [32] M. Abramowitz and I. A. Stegun, *Handbook of Mathematical Functions with Formulas, Graphs, and Mathematical Tables* (Dover, 1964) national Bureau of Standards Applied Mathematics Series 55.
- [33] I. J. Thompson and A. R. Barnett, *Comput. Phys. Commun.* **36**, 363 (1985).
- [34] J. R. Taylor, *Scattering Theory: The Quantum Theory of Nonrelativistic Collisions* (Wiley, 1972).
- [35] R. G. Newton, *Scattering Theory of Waves and Particles*, 2nd ed. (Springer, 1982).
- [36] M. Pillai, J. Goglio, and T. G. Walker, *Am. J. Phys.* **80**, 1017 (2012).
- [37] V. Sitzmann, J. N. P. Martel, A. W. Bergman, D. B. Lindell, and G. Wetzstein, in *Advances in Neural Information Processing Systems*, Vol. 33 (2020) pp. 7462–7473, arXiv:2006.09661.
- [38] A. D. Jagtap, K. Kawaguchi, and G. E. Karniadakis, *J. Comput. Phys.* **404**, 109136 (2020).
- [39] A. G. Baydin, B. A. Pearlmutter, A. A. Radul, and J. M. Siskind, *J. Mach. Learn. Res.* **18**, 1 (2018).
- [40] D. P. Kingma and J. Ba, in *3rd International Conference on Learning Representations (ICLR)* (2015) arXiv:1412.6980.
- [41] S. Wang, Y. Teng, and P. Perdikaris, *SIAM J. Sci. Comput.* **43**, A3055 (2021).
- [42] D. C. Liu and J. Nocedal, *Math. Program.* **45**, 503 (1989).
- [43] A. Paszke, S. Gross, F. Massa, A. Lerer, J. Bradbury, G. Chanan, T. Killeen, Z. Lin, N. Gimelshein, L. Antiga, A. Desmaison, A. Köpf, E. Yang, Z. DeVito, M. Raison, A. Tejani, S. Chilamkurthy, B. Steiner, L. Fang, J. Bai, and S. Chintala, in *Advances in Neural Information Processing Systems*, Vol. 32 (2019) arXiv:1912.01703.

- [44] S. Wang, S. Sankaran, and P. Perdikaris, arXiv preprint arXiv:2203.07404 (2022), computer Methods in Applied Mechanics and Engineering, submitted, [arXiv:2203.07404](#).
- [45] A. Boehnlein, M. Diefenthaler, N. Sato, S. Schramm, S. Sekula, I. Vitev, *et al.*, [Rev. Mod. Phys. **94**, 031003 \(2022\)](#).
- [46] I. J. Thompson, [Comput. Phys. Rep. **7**, 167 \(1988\)](#).
- [47] N. Austern, Y. Iseri, M. Kamimura, M. Kawai, G. Rautscher, and M. Yahiro, [Phys. Rep. **154**, 125 \(1987\)](#).
- [48] K. Hagino, K. Ogata, and A. M. Moro, [Prog. Part. Nucl. Phys. **125**, 103951 \(2022\)](#).
- [49] A. Deltuva, A. C. Fonseca, and P. U. Sauer, [Phys. Rev. C **71**, 054005 \(2005\)](#).
- [50] R. Lazauskas, [Phys. Rev. C **97**, 044002 \(2018\)](#).
- [51] S. Goswami, C. Anitescu, S. Chakraborty, and T. Rabczuk, [Theor. Appl. Fract. Mech. **106**, 102447 \(2020\)](#).
- [52] S. Chakraborty, [J. Comput. Phys. **426**, 109942 \(2021\)](#).
- [53] R. Lazauskas and J. Carbonell, [Few-Body Syst. **60**, 62 \(2019\)](#).